Carbon Capture Science & Technology 13 (2024) 100274

Contents lists available at ScienceDirect

Carbon Capture Science & Technology

journal homepage: www.elsevier.com/locate/ccst

Full Length Article

Zr-MOF/MXene composite for enhanced photothermal catalytic CO_2 reduction in atmospheric and industrial flue gas streams

Yang Meng[a,1], Feng Yue[a,1], Shuo Zhang[a], Lingji Zhang[a], Cong Li[b], Mengke Shi[a], Yongpeng Ma[a], Mario Berrettoni[b], Xiaojing Zhang[a,*], Hongzhong Zhang[a,*]

[a] Henan Collaborative Innovation Center of Environmental Pollution Control and Ecological Restoration, Zhengzhou University of Light Industry, Zhengzhou, 450001, China

[b] Department of Chemistry, University of Camerino, 62032, Camerino, Macerata, Italy

ARTICLE INFO

Keywords:
Zr-MOF/MXene
Photothermal catalytic
CO_2 reduction
Atmosphere
Industrial emissions

ABSTRACT

In this study, a novel composite was engineered by integrating Zr-MOF (NH_2-UIO-66) with MXene layers through electrostatic self-assembly. Under simulated sunlight and at 80 °C, this composite material achieved nearly complete conversion of low-concentration atmospheric CO_2 to CO and CH_4 without additional sacrificial agents or alkaline absorption liquids, marking one of the few reports demonstrating near-complete reduction of low-concentration CO_2 directly from the air. For high-concentration CO_2 in industrial flue gas, the composite utilized residual heat at 80 °C without additional energy input, exhibiting excellent CO_2 reduction efficiency with CO and CH4 production rates of 127 $\mu mol \cdot g^{-1} \cdot h^{-1}$ and 330 $\mu mol \cdot g^{-1} \cdot h^{-1}$, respectively, resulting in a total production rate 4.76 times higher than that in the air. Compared to most reports on thermocatalytic CO_2 reduction (>300 °C), this material shows significant advantages below 100 °C. The performance improvement is attributed to the introduction of Zr-MOF, which provides additional active sites and reduces activation energy. Additionally, the localized surface plasmon resonance (LSPR) effect of MXene facilitates the migration of thermal charge carriers to Zr^{4+} sites within the MOF. Density Functional Theory (DFT) calculations validate these findings. Overall, Zr-MOF/MXene composite holds potential for reducing CO_2 in air and industrial settings, advancing energy conversion and environmental management.

1. Introduction

Since the Industrial Revolution, human activities have substantially escalated the release of greenhouse gases into the atmosphere. (Muringa Kandy et al., 2021; He and Janáky, 2020) This heightened emission has resulted in an ongoing rise in greenhouse gas concentrations, intensifying the greenhouse effect and precipitating a range of global climate challenges, including global warming, glacier retreat, and rising sea levels. (Zhao et al., 2021) Therefore, there is an urgent need to explore effective ways to reduce carbon emissions or decrease CO_2 concentration in the atmosphere. (Gong et al., 2022; Zhai et al., 2023)

In this context, developing CO_2 resource utilization technology has become a key approach to addressing CO_2-related environmental issues and promoting the carbon cycle. (Shang et al., 2023; Guo et al., 2022) Currently, the utilization of CO_2 mainly revolves around CO_2 capture and storage, electrocatalysis, photocatalysis, and thermocatalysis technologies. (Dimitriou et al., 2015; Lim et al., 2022; Jiang et al., 2020) However, while CO_2 capture and storage technology is effective, its high energy consumption, cost, and potential leakage risks limit its widespread application. (Fang et al., 2023; Li et al., 2019) In contrast, treating CO_2 as a renewable carbon resource and converting it into high-value chemicals through electrocatalytic and photocatalytic reactions not only reduces dependence on fossil fuels but also has significant economic and environmental benefits. (Davis et al., 2020; Liu et al., 2022; Rehman et al., 2022) Therefore, converting CO_2 into clean fuels through catalytic reactions has become one of the important solutions for global emissions reduction. (J. Wang et al., 2022; Xiong et al., 2018; Qi et al., 2023) For example, Chen et al. demonstrated a hybrid approach by combining MOF with organolead halide compounds, adjusting crystallinity to merge the high surface area and porous structure of MOF with the excellent photocarrier transport properties of organolead halides. They developed the TMOF-10-NH_2 photocatalytic material, exhibiting remarkable activity with a CO production rate of 78 $\mu mol \cdot g^{-1} \cdot h^{-1}$ under pure CO_2 conditions. (Chen et al., 2022) Wang et al. developed bimetallic metal oxide nanosheets (Pd-CeO_2) doped with positively charged noble metals. The inclusion of Pd not only improved water activation, provid-

* Corresponding authors.
E-mail addresses: zhangxj@iccas.ac.cn (X. Zhang), zhz@zzuli.edu.cn (H. Zhang).
[1] These authors contributed equally to this work and should be considered co-first authors.

https://doi.org/10.1016/j.ccst.2024.100274
Received 22 June 2024; Received in revised form 6 August 2024; Accepted 6 August 2024

ing more protons, but also enhanced the conductivity of material, facilitating the separation and transfer of photogenerated carriers. This innovative approach resulted in a CH_4 production rate of 41.6 μmol·g^{-1}·h^{-1} under pure CO_2 conditions. (Z. Wang et al., 2022)

However, most current research on CO_2 reduction focuses on using high-purity CO_2 or specific hydrogenation conditions, with relatively fewer studies on the direct catalytic reduction of low-concentration CO_2 in the atmosphere. (Zhao et al., 2021; Chen et al., 2020; Wu et al., 2021; Zhou et al., 2021; Crake et al., 2017; Z. Wang et al., 2022; Han et al., 2022; Low et al., 2018) The atmospheric CO_2 concentration is approximately 0.04 %, which significantly increases the difficulty of activating CO_2 and requires more active catalysts and precise reaction condition control. (Ma et al., 2023; Yue et al., 2024) Moreover, the presence of atmospheric components such as oxygen and nitrogen may affect the selectivity of the catalytic reaction. (Schäppi et al., 2021; Zoller et al., 2022) With increasing concern over climate change and the development of green sustainable chemistry, directly capturing and catalytically reducing CO_2 from the atmosphere has become an imperative trend, aiming to improve the efficiency and economy of low-concentration CO_2 reduction. (Fang et al., 2023)

Industrial flue gas, as the main source of anthropogenic CO_2 emissions, has varying CO_2 concentrations (2 %~29 %) in electricity, steel, cement, and other industries' flue gases. (Wang et al., 2021; Wu et al., 2020; Yuan et al., 2021; Liao et al., 2021) Currently, the treatment of CO_2 in industrial flue gas mainly relies on absorption, adsorption, membrane separation, and cryogenic separation technologies, which mostly focus on CO_2 separation and capture, rather than directly converting CO_2 into valuable chemicals. (Liu et al., 2024; Gun et al., 2023) Furthermore, industrial flue gas emissions often accompany residual heat. Leveraging this energy to activate catalysts and facilitate CO_2 reduction in flue gases could present a novel and efficient approach to CO_2 treatment.

Considering these challenges and opportunities, this study aims to develop an innovative catalyst for the photothermocatalytic reduction of both low-concentration CO_2 in the atmosphere and higher-concentration CO_2 in industrial flue gases. Through electrostatic self-assembly methods, Zr-MOF (NH_2-UIO-66) will be integrated into the layered molecular structure of MXene. Under simulated sunlight conditions at 80 °C, the Zr-MOF act as the catalytic active site, (Trickett et al., 2017; Tian et al., 2019) utilizing the LSPR effect and high conductivity of MXene to photothermocatalytically reduce CO_2 in the atmosphere and industrial flue gas, (Wu et al., 2021; Zhuang et al., 2023; Venkateswarlu et al., 2023; Huang et al., 2023) effectively converting it into valuable gaseous fuels such as CH_4 and CO. This research has profound implications for addressing environmental challenges and the energy crisis, offering significant opportunities for energy conservation, emissions reduction, and the advancement of a low-carbon economy.

2. Experimental

2.1. Synthesis and characterization

See supplementary information for details.

2.2. Photothermal catalytic CO_2 reduction process

Reduction of CO_2 in the atmosphere: The 5 mg Zr-MOF/MXene catalyst sample was placed in a 160 mL reaction vessel, followed by the addition of 1 mL of distilled water, and then the vessel was sealed. A 300 W Xe lamp, designed to mimic sunlight (AM 1.5 G), was employed along with external water bath circulation to regulate the reaction temperature (Fig. 1). The catalytic performance of the material was assessed for CO_2 reduction under different conditions, including light irradiation, varied temperatures, and photothermal synergistic conditions. Gas samples (1 mL) were withdrawn from the reaction vessel every hour using a gas-tight syringe and subjected to analysis by gas chromatography (GC-7980) to measure the concentration of CO_2 reduction products.

Reduction of CO_2 in industrial flue gas: A mixture of gases with a 10 % CO_2 vol fraction was prepared using air as the background, simulating industrial flue gas. The experimental steps were the same as those for the reduction of CO_2 in the atmosphere.

2.3. Theoretical calculations

DFT calculations were utilized to delve deeper into the reaction mechanism underlying the catalytic reduction of CO_2 by Zr-MOF/MXene. The specific parameters employed in the DFT simulations are outlined in the supplementary information.

3. Results and discussion

3.1. Structure and microscopic morphology analysis

XRD analysis was employed to investigate the crystal structure of Zr-MOF, MXene, and MOF/MXene composites. As shown in Fig. 2A, two diffraction peaks can be observed at around 19° and 62° for MXene, corresponding to the (004) and (110) characteristic crystal planes of MXene, respectively. (Huang et al., 2023) The MOF/MXene composites with different MOF loadings display three diffraction peaks at 4.5°, 20°, and 62°, which align with the diffraction peak of MOF near 5° and the diffraction peaks of MXene at 19° and 62° This result indicates that MOF and MXene have been successfully combined.

Given the high specific surface area and exceptional porosity of MOF materials, they possess the capability to adsorb CO_2 from the atmosphere to extent. (Pang et al., 2023) This implies that in our catalytic reaction system, CO_2 sources can be categorized as CO_2 directly from the air and CO_2 adsorbed by MOF/MXene composite materials. To accurately evaluate the overall CO_2 content in the reaction system, we examined the specific surface area and CO_2 adsorption-desorption properties of the 6 % MOF/MXene composite material (Fig. 2B). The results show that under the conditions of 25 °C and a relative pressure P/P_0=1 (standard atmospheric pressure), the adsorption capacity of the composite material for CO_2 is 0.2539 cm^3/g. Based on this, we calculated that the 6 % MOF/MXene composite material provides 8 ppm of CO_2 within the reaction apparatus, coupled with the inherent 410 ppm of CO_2 in the air, the total concentration of CO_2 within the reaction system amounted to 418 ppm. Moreover, the BET specific surface area of the 6 % MOF/MXene composite material is 1.72 m^2/g, notably lower than that of pure Zr-MOF (Figure. S1). (Liu et al., 2021) This reduction in surface area is mainly due to the lower MOF content in the composite material, resulting in decreased specific surface area compared to pure MOF, which in turn affects its CO_2 adsorption capacity.

Utilizing SEM, TEM, and EDS to further investigate the microstructure and elemental distribution on the surface of the material. The Zr-MOF exhibits a porous structure formed by particulate aggregation, while the MXene displays a characteristic 2D layered configuration with a smooth surface devoid of impurity particles (Fig. 3A-B). Figs. 3C-D illustrate the distribution of Zr-MOF particles on the surface and between the layers of MXene. Additionally, the EDS point scan, line scan, and mapping images (Figures. S2–3) reveal the presence of Zr, Ti, F, O, C, and N elements in the composite material, all of which are uniformly distributed. Further examination using TEM imaging (Fig. 3E-F) confirms the successful loading of MOF particles on the MXene surface and between its layers. High-resolution images reveal lattice fringes (marked in yellow) of the MOF/MXene composite with a lattice spacing (d) of 0.26 nm, corresponding to the (110) crystal plane of MXene. These observations collectively confirm the effective embedding of MOF particles into MXene 2D layered structure via electrostatic self-assembly, consistent with XRD measurements.

XPS further characterized the composition and chemical states of MOF, MXene, and the MOF/MXene composite. Characteristic peaks of

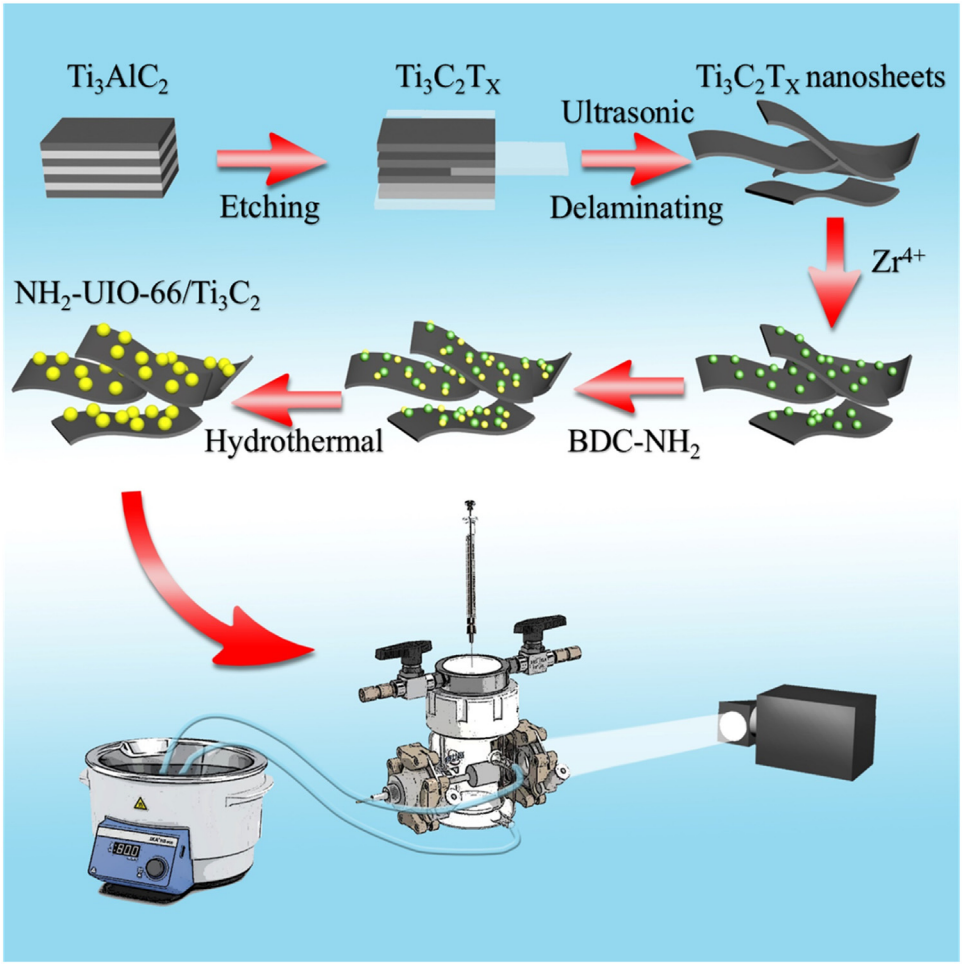

Fig. 1. Preparation scheme of Zr MOF/MXene and CO_2 reduction reaction scheme.

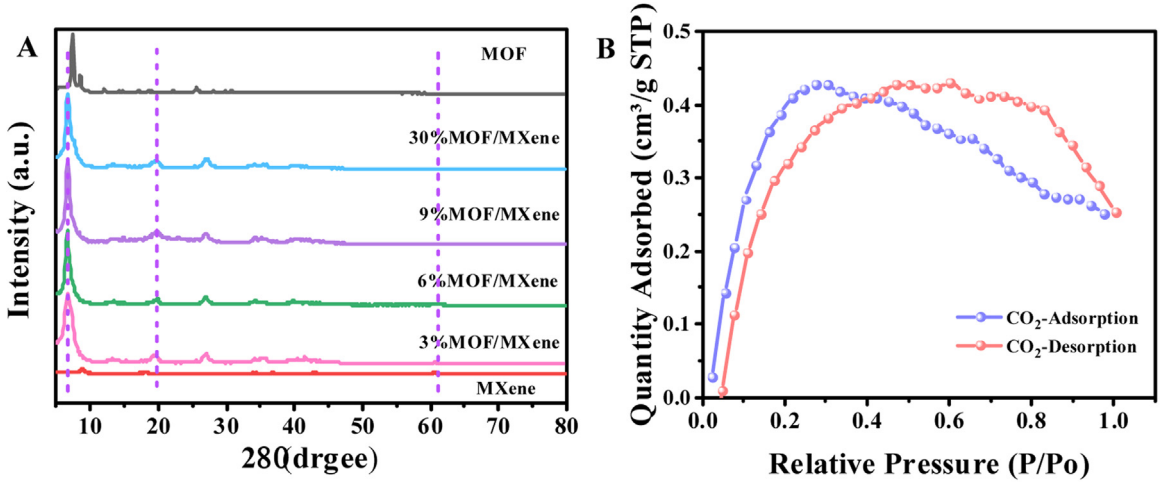

Fig. 2. A. XRD patterns of MOF, MXene, and MOF/MXene; B. CO_2 adsorption-desorption curve of 6 % MOF/MXene.

Zr, N, O, and C are observed for MOF, while Ti, O, C, and F peaks are present for MXene. The MOF/MXene composite exhibits all of these peaks, albeit with variations in relative intensities (Fig. 4A). The C 1 s spectrum (Fig. 4B) of the MOF/MXene composite exhibits distinct peaks at 288.8 eV, 286.2 eV, 284.8 eV, and 281 eV, corresponding to various bonds including C = O (288.7 eV) and C–O (286.2 eV) from MOF, and C–C (284.8 eV), C-F (288.8 eV), and Ti-C (281 eV) from MXene. Notably, the intensity of the Ti-C peak is slightly reduced compared to pure MXene, potentially due to the introduction of MOF. In the Ti 2p spectrum (Fig. 4C), six peaks at 454.8 eV, 456.3 eV, 458.5 eV, 460.7 eV, 462.1 eV, and 463.9 eV indicate different orbitals of Ti in MXene, with slight shifts compared to pure MXene due to MOF-MXene interactions. The O 1 s spectrum (Fig. 4D) reveals peaks at 528.9 eV, 532 eV, and 533.3 eV, corresponding to C–O and C = O from MOF, and Ti-O, C-Ti-Ox, and C-Ti-OHx from MXene. The decrease in intensity and shift in the position of the Ti-O peak indicate a slight alteration in the chemical environment

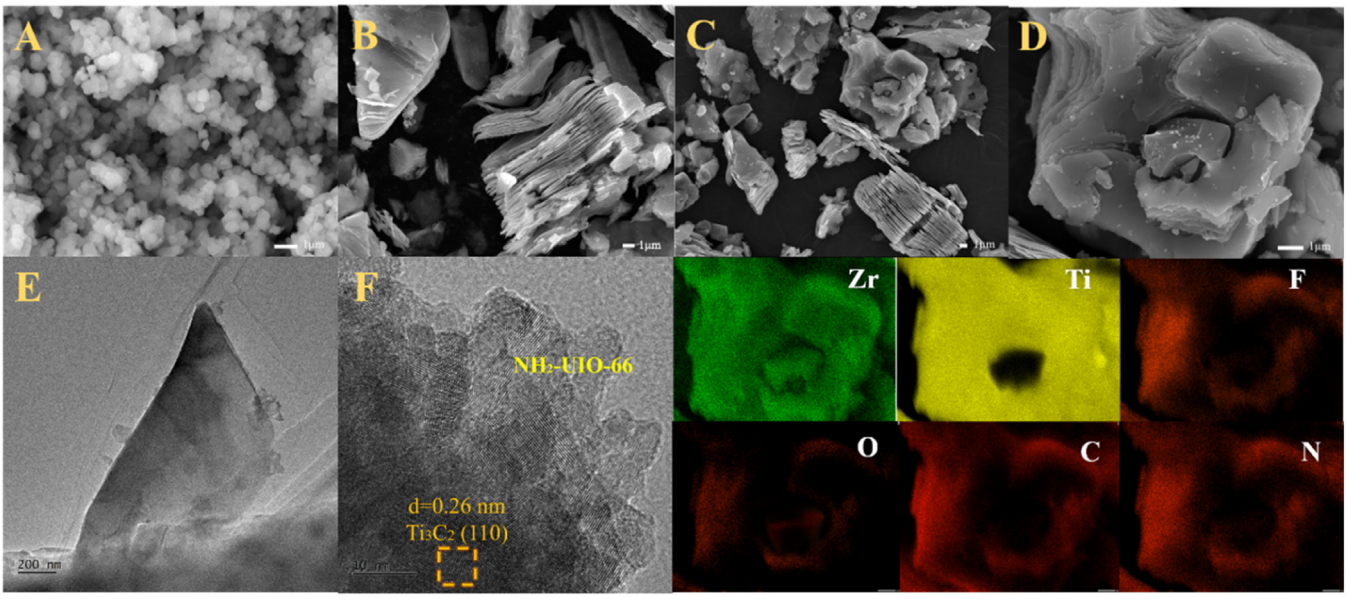

Fig. 3. SEM images (A. MOF; B. MXene; C-D. 6 % MOF/MXene), HRTEM images of 6 % MOF/MXene (E-F).

of O atoms due to the combination of MOF and MXene. The F 1 s spectrum (Fig. 4E) displays peaks at 684.3 eV and 685.7 eV, attributed to F-Ti and F-C bonds from MXene. In the Zr 3d and N 1 s spectra (Fig. 4F-G), peaks at 182.9 eV, 185.4 eV, and 400.3 eV indicate Zr-O orbitals and -NH_2 groups from MOF. The shift in the binding energy of Zr 3d from 182.8 eV to 182.5 eV indicates an increase in the electron density of Zr after loading the MOF onto the MXene structure. This change is attributed to the transfer of electrons from MXene to the metal center Zr^{4+} in the MOF. Overall, the XPS spectra of the MOF/MXene composite demonstrate a combination of characteristic features from both MOF and MXene, as well as evidence of chemical interactions between the two materials.

Fig. 5A shows the Raman spectra of MOF, MXene, and MOF/MXene composites. It is evident that the MOF does not exhibit distinct characteristic peaks. The strong peak at 149 cm^{-1} is attributed to the resonant peak of MXene. The peak at 390 cm^{-1} corresponds to the E_g mode vibrations of MXene (in-plane vibrations, Ti-OH), while the peak at 503 cm^{-1} is related to out-of-plane bending vibrations associated with OH (Ti-OH). The peak at 625 cm^{-1} is due to vibrations related to the C element in MXene (including E_g and A_{1g} modes). Peaks at 1376 and 1557 cm^{-1} are attributed to the D and G bands of carbon, also originating from the C element in MXene. After compositing with Zr-MOF, the resonant peak of MXene at 147 cm^{-1} significantly weakens; the characteristic peaks at 265, 402, and 608 cm^{-1}, representing in-plane bending vibrations of titanium atoms with surface groups (E_g) and vibrations of carbon atoms (E_g and A_{1g}), are significantly enhanced. This suggests interactions between Zr-MOF and MXene materials. No new distinct characteristic peaks appear, indicating that the interactions are likely not due to chemical bonding but rather electronic interactions.

The optical properties of different materials were tested using UV–Vis. As shown in Fig. 5B, it can be observed that MOF exhibits a distinct absorption edge at 447 nm. Furthermore, within the wavelength range of 250 nm to 420 nm, the absorbance of MOF is significantly higher than that of MXene and MOF/MXene composites. This indicates that MOF has greater responsiveness to low-wavelength light. On the other hand, MXene shows remarkable light absorption performance without any clear absorption edge within the 250 nm to 800 nm wavelength range, consistent with its metallic characteristics. For the MOF/MXene composites of different ratios, it was noted that within the 250 nm to 420 nm wavelength range, the composite materials displayed slightly superior light absorption performance compared to MXene alone. This enhancement could be attributed to the introduction of MOF, increasing light absorption in the lower wavelength segment of the composite, aligning with the characteristic light responsiveness of MOF. However, the overall light absorption profile of the composites remains similar to MXene, with no significant absorption edges, suggesting that the introduction of MOF does not alter the metallic-like properties of MXene.

These findings imply that while MOF/MXene composites may have limited capability to generate photogenerated charge carriers under direct illumination, the distinctive photothermal conversion characteristics, high conductivity, and LSPR effect of MXene could facilitate the rapid migration of thermal charge carriers to MOF and the adsorbed reactants when the external temperature is increased. (Huang et al., 2023) This process is expected to provide more reactive sites for CO_2 reduction, thereby enhancing the efficiency of photo-thermal synergistic reduction of CO_2.

3.2. *Photothermal catalytic reduction of atmospheric CO_2 performance*

Fig. 6A-C present the evaluation performance of MOF, MXene, and MOF/MXene composite materials with different proportions in the photocatalytic reduction of atmospheric CO_2 under room temperature (25 °C) and simulated sunlight illumination conditions (AM 1.5 G). The findings reveal that pure MXene exhibits relatively weak CO_2 reduction capabilities, and the catalytic product is a mixture of CO and CH_4. Conversely, MOF demonstrates excellence catalytic reduction performance, and the catalytic products show high selectivity for CO. The difference in product selectivity is attributed to the difference in electronic properties between the two. For MOF/MXene composite materials, significant CH_4 production was observed at low MOF loading, and the catalytic ability was improved with increasing MOF loading. The optimal photocatalytic performance was achieved at 30 % MOF loading, producing 264 $\mu mol \cdot g^{-1}$ of CO within 6 h at a rate of 44 $\mu mol \cdot g^{-1} \cdot h^{-1}$, surpassing the reduction performance of MXene alone.

MXene possesses excellent thermal effects, the presence of heat energy can induce numerous charge carriers and increase charge transfer rates. Additionally, the introduction of heat may alter the catalytic reaction pathways on the MXene surface or lower the activation energy required for the reaction, further improving the catalytic performance. (Xu et al., 2020) Therefore, we employed a thermostatic water bath circulation method to assess the CO_2 reduction capabilities of MOF, MXene, and MOF/MXene composites with different ratios at 80 °C

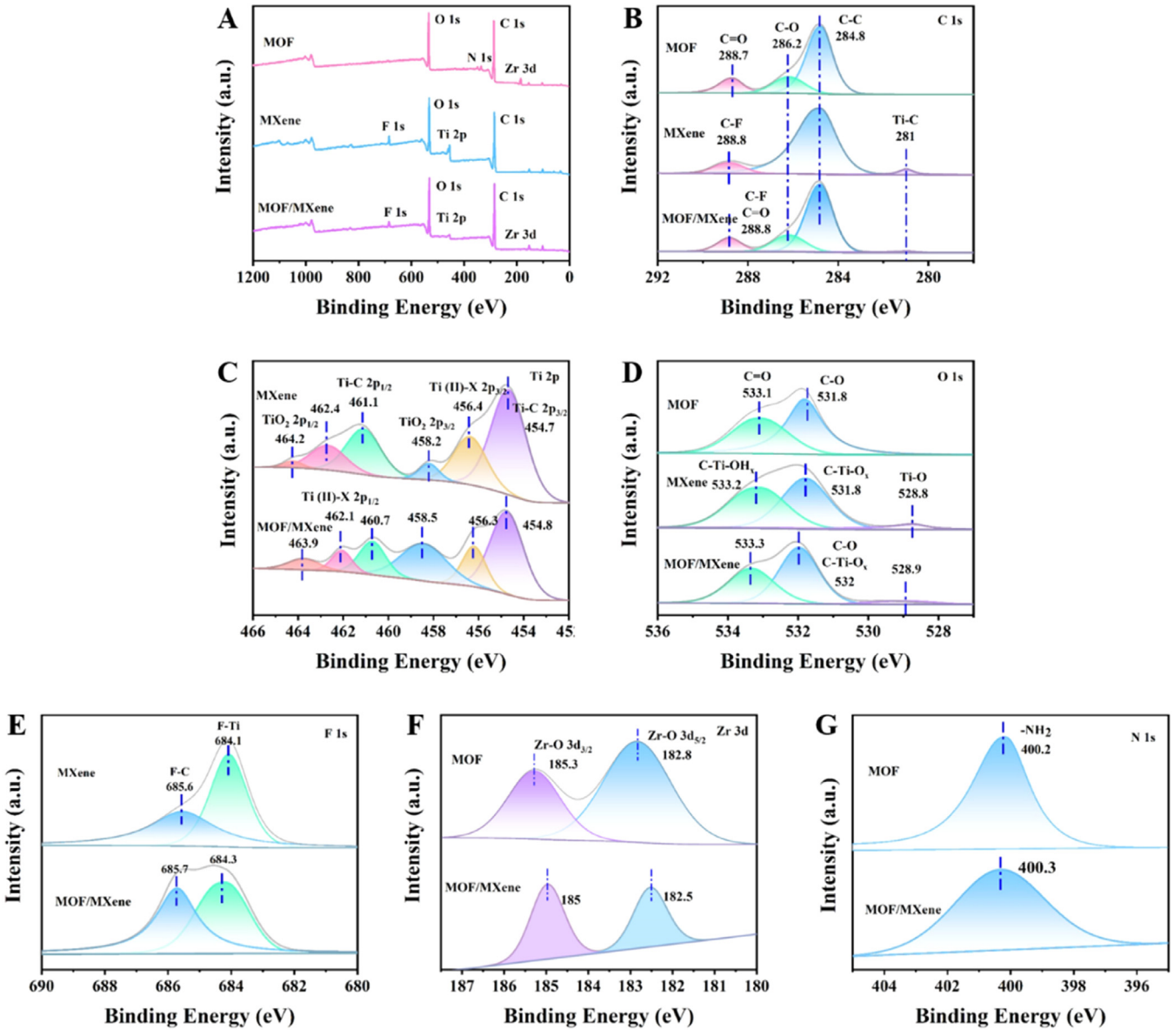

Fig. 4. XPS spectrum of MOF, MXene and MOF/MXene. A. survey spectrum; B. C1s; C. Ti 2p; D. O 1 s; E. F 1 s; F. Zr 3d; G. N 1 s.

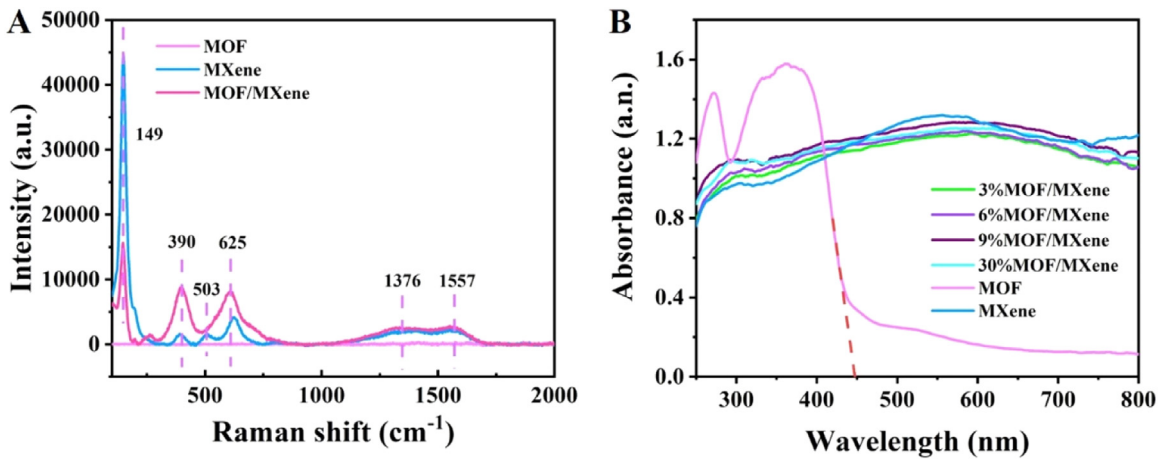

Fig. 5. A. Raman spectra; B. UV–Vis DRS of MOF, MXene and MOF/MXene.

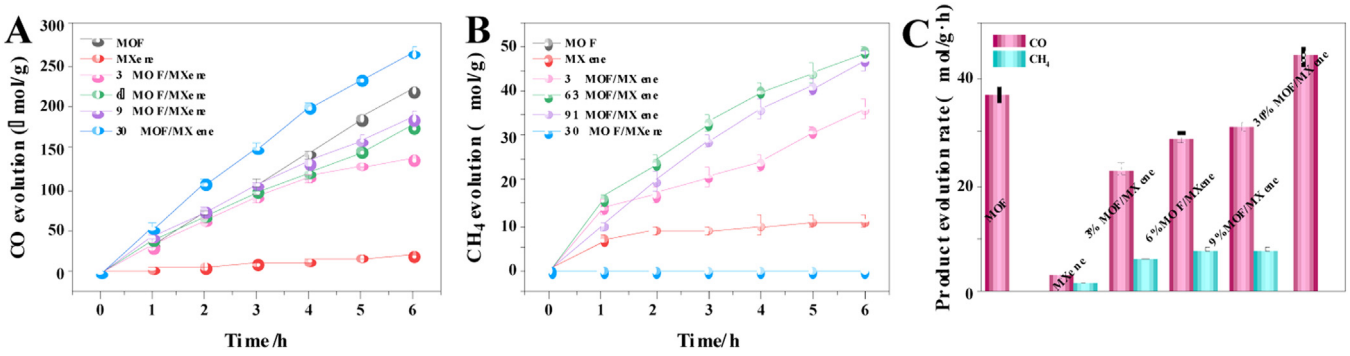

Fig. 6. Product evolution diagram: A. CO; B. CH_4; C. CO and CH_4 evolution rate.

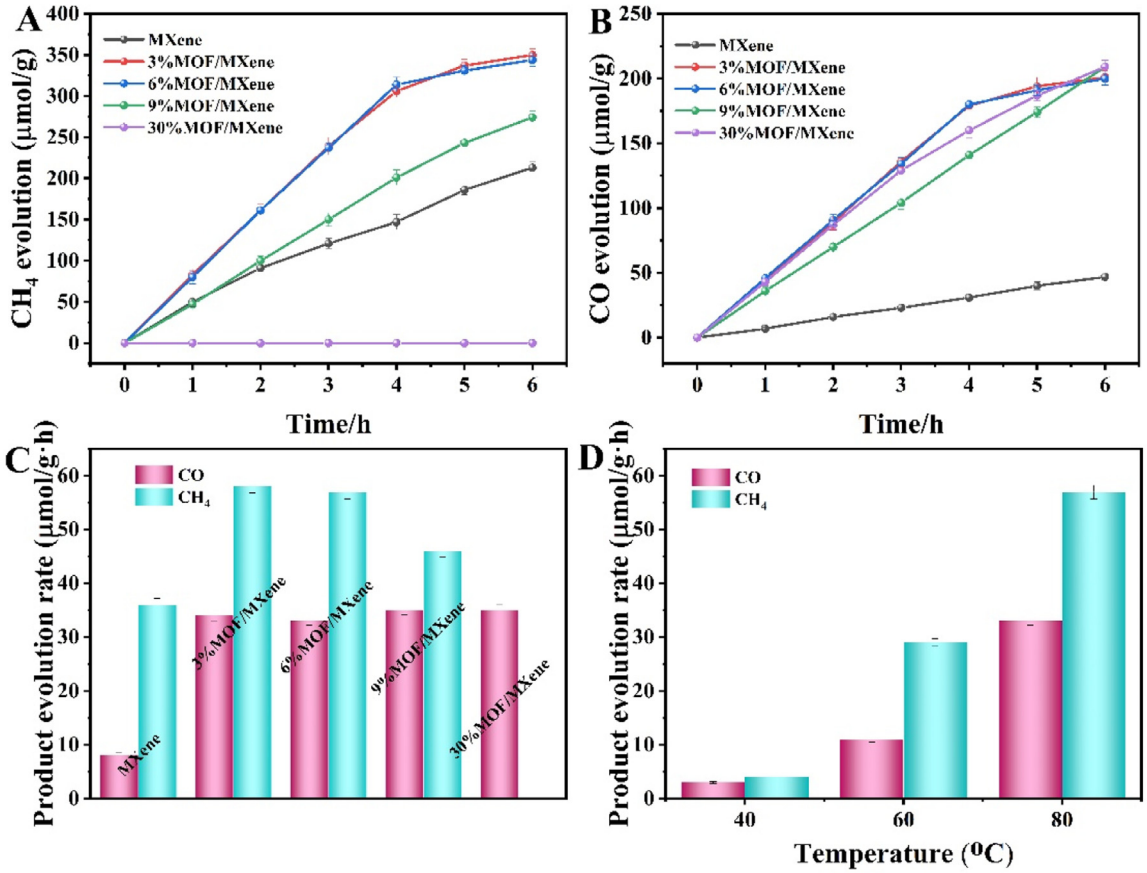

Fig. 7. Product evolution diagram: A. CH_4; B. CO; C. CO and CH_4 evolution rate; D. CO and CH_4 evolution rate at different temperatures.

without light irradiation, as shown in Fig. 7A-C. It was found that MOF has no thermal catalytic performance, and pure MXene exhibited some thermal catalytic ability. The catalytic activity is significantly enhanced when a lower proportion of MOF is supported in the structure of MXene. For example, the 6 % MOF/MXene composite exhibits the highest thermal catalytic performance, producing 201 $\mu mol \cdot g^{-1}$ of CO and 350 $\mu mol \cdot g^{-1}$ of CH_4 within 6 h, with production rates of 34 $\mu mol \cdot g^{-1} \cdot h^{-1}$ and 58 $\mu mol \cdot g^{-1} \cdot h^{-1}$, respectively, achieving a total product generation rate of 92 $\mu mol \cdot g^{-1} \cdot h^{-1}$. In our experimental setup, with an initial CO_2 concentration of 418 ppm, the resulting concentrations of CO and CH_4 reached 140 ppm and 241 ppm, respectively. This suggests that the composites at these ratios achieved nearly complete reduction of low-concentration CO_2 from the air under thermal catalysis at 80 °C. To our knowledge, this represents the first reported instance of near-complete reduction of low-concentration CO_2 directly from the atmosphere. In summary, the addition of an appropriate amount of MOF enables MXene-based composites to exhibit exceptional thermal catalytic CO_2 reduction performance. This is attributed to the increased availability of reactive sites provided by MOF for CO_2 reduction. Moreover, under high-temperature conditions, the hot charge carriers excited by the LSPR effect of MXene can rapidly transfer to the Zr^{4+} metal centers of MOF and likely lowers the activation energy of the thermal catalytic CO_2 reduction reaction, accelerating the catalytic process.

Combining with the sunlight illumination experiments, the 6 % MOF/MXene composite material displayed the best CO_2 reduction performance under both light and 80 °C conditions. Therefore, we further tested the catalytic activity of this composite at a temperature gradients (Fig. 7D). The catalytic performance of the 6 % MOF/MXene composite significantly improved with increasing temperature, the total CO and CH_4 production rate at 80 °C being 2.3 times that at 60 °C and 13.1

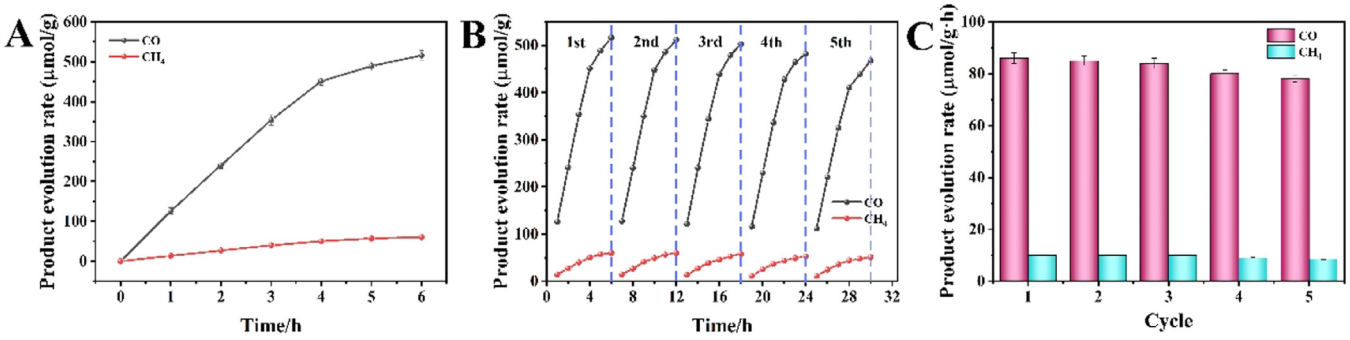

Fig. 8. 6 % MOF/MXene: A. CH_4 and CO evolution diagram; B. Five-cycle stability diagram; C. CH_4 and CO evolution rate diagram.

times that at 40 °C, further confirming the thermal catalytic advantage of MXene-based composite.

Photocatalytic and thermocatalytic tests of MOF, MXene, and MOF/MXene composite materials reveal that MOF possesses superior photocatalytic activity, while MXene excels in thermocatalytic reactions. Building upon this, we conducted simulations on the photothermal synergistic catalytic reduction of CO_2 in ambient air and assessed the catalytic stability of the 6 % MOF/MXene composite under 80 °C and sunlight irradiation, as depicted in Fig. 8A-C. The experimental outcomes illustrate a substantial enhancement in CO_2 reduction efficiency under photothermal synergy, where the combined production rate of CO and CH_4 exceeds that under individual sunlight or thermal conditions. Within 6 h, the yield and production rate of CO reach 516 $\mu mol \cdot g^{-1}$ and 86 $\mu mol \cdot g^{-1} \cdot h^{-1}$, while CH_4 reaches 60 $\mu mol \cdot g^{-1}$ and 10 $\mu mol \cdot g^{-1} \cdot h^{-1}$, respectively. The total product production rate amounts to 96 $\mu mol \cdot g^{-1} \cdot h^{-1}$, representing a 2.56-fold increase compared to sunlight irradiation alone and a 1.04-fold increase compared to 80 °C thermal conditions. Converted to the concentration within the reaction system, CO reaches 361 ppm and CH_4 reaches 42 ppm, the a total product concentration of 403 ppm, indicating nearly complete reduction of CO_2 in the air. Furthermore, comparing with the thermocatalytic results, a significant shift in CO_2 reduction products is observed. The primary product in the thermocatalytic process is CH_4, with a CH_4:CO molar ratio of 1.74:1. In contrast, the main product in the photothermal synergistic catalysis is CO, with a CH_4:CO molar ratio of 1:8.6. This phenomenon indicates the composite material excellent product selectivity under different experimental conditions. Through five consecutive cycles of reaction tests, the composite material exhibits remarkable catalytic stability, with the catalytic effect remaining above 90 % of the initial reaction, thereby providing solid experimental evidence for the application of this composite material in the conversion of low-concentration atmospheric CO_2.

To confirm the carbon source, we enforced three control experiments: sunlight + 80 °C, atmosphere + water vapor, without catalyst (Fig. 9A); sunlight + 80 °C, N_2 + water vapor, with catalyst (Fig. 9B); and sunlight + 80 °C, O_2 + water vapor, with catalyst (Fig. 9C). No significant product formation was observed under any of these conditions. Additionally, we conducted a ^{13}C isotope labeling experiment (Fig. 9D). Using atmospheric CO_2 concentration as a baseline, a specific quantity of $^{13}CO_2$ was introduced into the reactor for testing, and a significant amount of $^{13}CH_4$ and ^{13}CO products were detected. These results confirm that the photothermal catalytic products CH_4 and CO are indeed derived from the conversion of atmospheric CO_2.

We further investigated the thermal stability of the material and examine the intermediates in the CO_2 reduction reaction process through thermogravimetric-infrared (TG-IR) tests under atmospheric conditions. The results indicate that 6 % MOF/MXene possesses excellent thermal stability, with a weight loss rate of 3.89 % between 30 and 200 °C (Fig. 9E). This loss is due to the evaporation of water and residual solvents from the preparation process. In the in situ infrared spectrum (Fig. 9F-G), several characteristic peaks can be identified: the 3200–3600 cm^{-1} region corresponds to the stretching vibrations of O–H bonds, while peaks in the 2850–3000 cm^{-1} range are attributed to C–H stretching vibrations. The peak around 2350 cm^{-1} is indicative of the asymmetric stretching of CO_2, and the 2100–2140 cm^{-1} range shows the stretching vibrations of CO. Peaks between 1700 and 1750 cm^{-1} represent the stretching vibrations of C = O bonds. Additionally, the 1200–1400 cm^{-1} range contains bending vibrations of O–H, and the 1000–1300 cm^{-1} range corresponds to the stretching vibrations of C–O bonds. These characteristic peaks suggest the presence of various intermediates such as CH_2^*, CH_3^*, CO, COOH*, CHO*, COH*, and CHOH* during the CO_2 reduction process. The concentration of these intermediates significantly increases with time and temperature, indicating the progressive nature of the reduction reaction. These findings not only underscore the stability of material under thermal conditions but also provide critical support for our theoretical calculations, exploring the CO_2 reduction reaction pathway.

3.3. Photothermal catalytic reduction performance of CO_2 in industrial flue gas

Taking into account the residual heat carried by industrial flue gas emissions, this study simulated the photothermal catalytic reduction performance of MXene and MOF/MXene composites for CO_2 in industrial flue gas (with a CO_2vol fraction of 10 %) under 80 °C conditions (Fig. 10A-C). The outcomes demonstrate that the 6 % MOF/MXene composite exhibits the most outstanding performance, with CO and CH_4 production rates far exceeding the reduction efficiency of CO_2 in air. Within 6 h, CO production reached 759 $\mu mol \cdot g^{-1}$ with a production rate of 127 $\mu mol \cdot g^{-1} \cdot h^{-1}$, while CH_4 production was 1979 $\mu mol \cdot g^{-1}$ with a production rate of 330 $\mu mol \cdot g^{-1} \cdot h^{-1}$. This resulted in a total product production rate of 457 $\mu mol \cdot g^{-1} \cdot h^{-1}$, marking a 4.97-fold increase in CO_2 reduction efficiency compared to atmospheric conditions. Additionally, to assess the composite material stability in catalyzing CO_2 reduction in industrial flue gas, we conducted five cycling tests (Fig. 10D). After five cycles, CO yield within 6 h was 685 $\mu mol \cdot g^{-1}$ with a production rate of 114 $\mu mol \cdot g^{-1} \cdot h^{-1}$, and CH_4 yield was 1810 $\mu mol \cdot g^{-1}$ with a production rate of 301 $\mu mol \cdot g^{-1} \cdot h^{-1}$. The total product production rate was 415 $\mu mol \cdot g^{-1} \cdot h^{-1}$, with catalytic performance at 90.8 % of the initial reduction, consistent with the cyclic stability observed in CO_2 reduction from air.

Additionally, compared to most previous reports on thermocatalytic CO_2 reduction (Table. 1), which typically require temperatures above 300 °C to activate CO_2 molecules, our MOF/MXene composite material exhibits significant temperature advantages. These conventional methods necessitate substantial energy input to achieve the high temperatures needed for CO_2 reduction. In contrast, our composite material can efficiently utilize the residual heat from industrial flue gas emissions, operating effectively below 100 °C. This demonstrates the remarkable efficiency of the composite at lower temperatures.

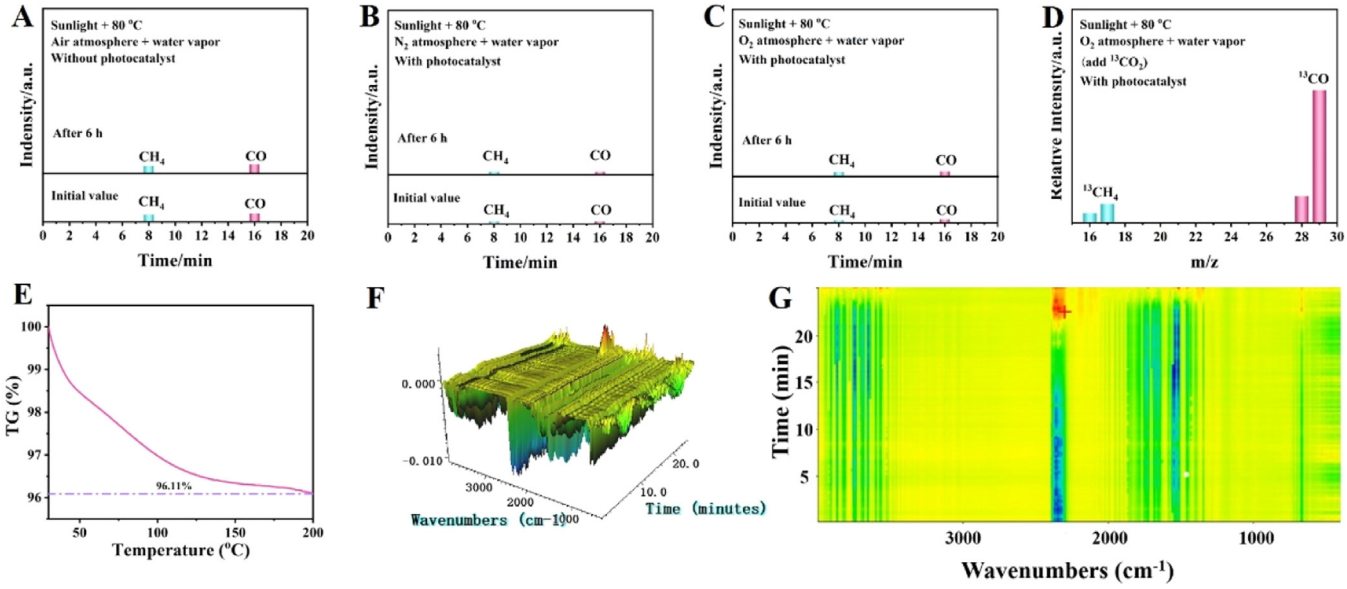

Fig. 9. A-C. Control experiments; D. ^{13}C Isotope labeling experiment; E-F. TG-IR spectra of 6 % MOF/MXene.

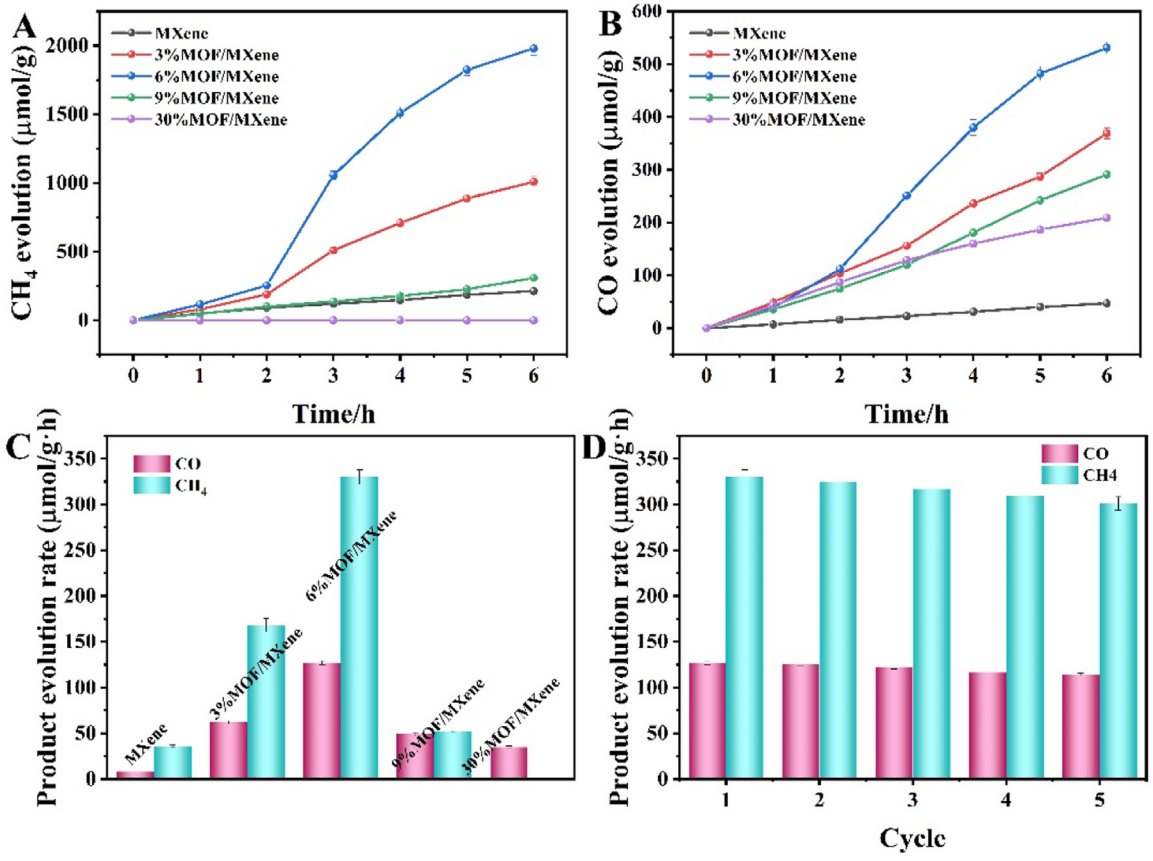

Fig. 10. Product evolution diagram: A. CH_4; B. CO; C. CO and CH_4 evolution rate; D. Five-cycle stability diagram of 6 % MOF/MXene.

In summary, the 6 % MOF/MXene composite not only performs excellently in the reduction conversion of low-concentration CO_2 in the air but also shows good thermocatalytic reduction and cyclic stability for industrial flue gas with higher CO_2 concentrations. This discovery offers a novel approach for effectively addressing CO_2 in both atmospheric and industrial flue gas settings, potentially advancing carbon cycle objectives.

3.4. Photothermal catalytic mechanism

Utilizing DFT, we explored the mechanism of thermocatalytic CO_2 reduction using Zr-MOF/MXene composite materials. Due to current technological limitations, we were unable to simulate the molecular configuration of Zr-MOF/MXene. To more closely approximate the actual configuration, we used the ZrOx structure present in the Zr-MOF molec-

Table. 1
Recent literature reports on thermal catalytic CO_2 reduction.

Catalyst	Reaction temperatures (℃)	Production rate	Ref
3DOM-LSCF	350	CH_4: 71 μmol·g^{-1}·h^{-1}	(Ha et al., 2016)
Ni-CeO_2	290	CH_4: 1.28 mmol·g^{-1}·h^{-1}	(Yang et al., 2023)
$Pt^0$2-MOF	140	CH_4: 188 μmol·g^{-1}·h^{-1}	(Mon et al., 2018)
TiFe/C	375	CO: 3.08 mmol·g^{-1}·h^{-1}	(Castells-Gil et al., 2021)
$NiFe_2O_4$	350	CH_4: 71.52 mmol·g^{-1}·h^{-1}	(Liu et al., 2016)
1.0-Ni-CeO_2	300	CO: 14.82 mmol·g^{-1}·h^{-1}	(Shen et al., 2022)
ZrO_2/Cu-ZnO	230	CO: 17.55 mmol·g^{-1}·h^{-1} CH_3OH: 15.61 mmol·g^{-1}·h^{-1}	(Stangeland et al., 2021)
Ru-TiO_2	200	CH_4: 7.38 mmol·g^{-1}·h^{-1}	(Kim et al., 2019)
Cu-Al_2O_3	600	CO: 176.42 mmol·g^{-1}·h^{-1}	(Bahmanpour et al., 2019)
Cu/β-Mo_2C	600	CO: 506.13 mmol·g^{-1}·h^{-1} CH_4: 5.11 mmol·g^{-1}·h^{-1}	(Zhang et al., 2016)
PtCo/TiO_2	300	CO: 21.43 mmol·g^{-1}·h^{-1} CH_4: 0.22 mmol·g^{-1}·h^{-1}	(Kattel et al., 2016)
Zr-MOF/MXene	80	CO: 127 μmol·g^{-1}·h^{-1} CH_4: 330 μmol·g^{-1}·h^{-1}	This work

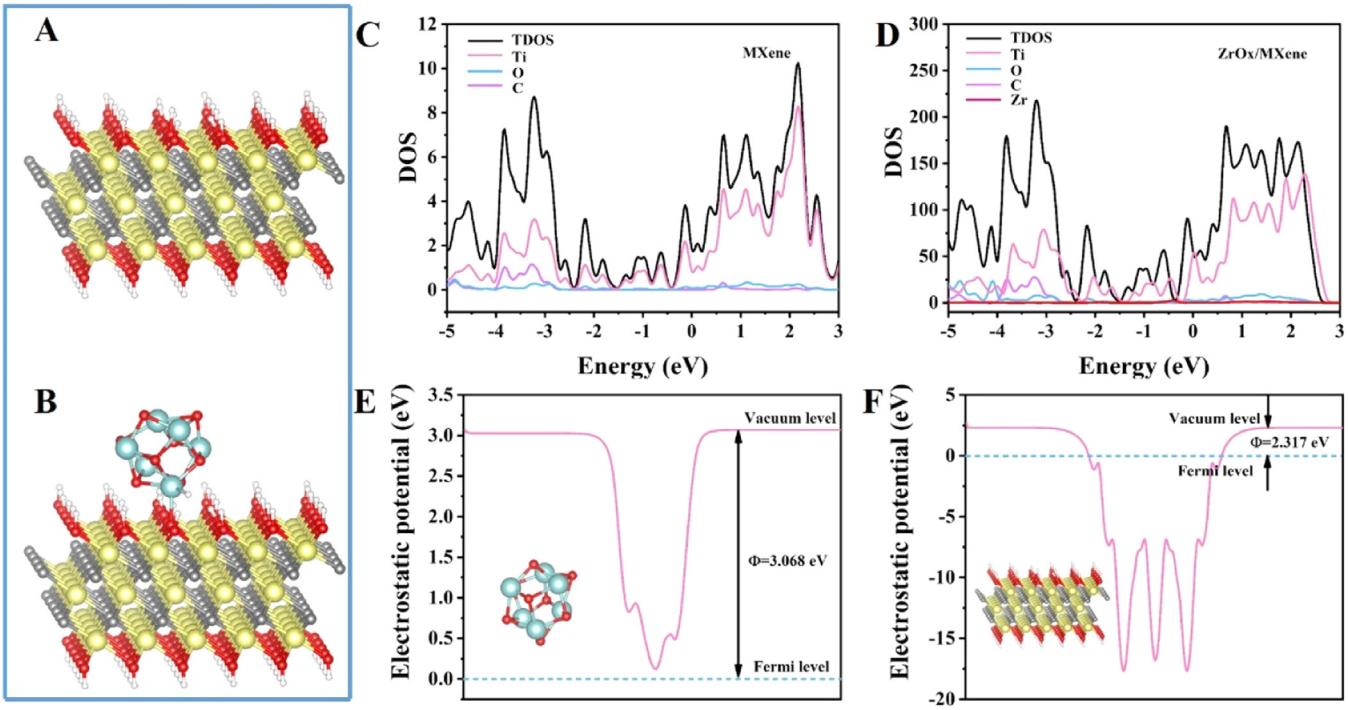

Fig. 11. Molecular structure: A. MXene; B. ZrOx/MXene. DOS: C. MXene; D. ZrOx/MXene. Calculated electrostatic potential: E. ZrOx; F. MXene.

ular configuration (Figure. S4) as a substitute model. Based on this, we constructed the molecular structures of MXene and ZrOx/MXene (Figs. 11A-B) and proceeded to calculate their density of states (DOS), work functions, reaction pathways, and Gibbs free energy. Our findings indicate that the DOS profiles of MXene and ZrOx/MXene are similar (Fig. 11C-D), with the Fermi level electronic states being fully occupied, demonstrating that the introduction of ZrOx does not alter the metallic-like nature of MXene. This is consistent with UV–Vis spectroscopy results. The work functions for ZrOx and MXene were determined to be 3.068 eV and 2.317 eV respectively (Fig. 11E-F), suggesting that electrons transfer from MXene to ZrOx, in agreement with the conclusions from XPS and the LSPR effect of MXene.

The CO_2 reduction reaction pathway, depicted in Fig. 12A and Figure. S5, follows the sequence $CO_2 + H^* \rightarrow COOH^* \rightarrow CO^* \rightarrow CHO^*$ or $COH^* \rightarrow CHOH^* \rightarrow CH^* \rightarrow CH_2{}^* \rightarrow CH_3{}^* \rightarrow CH_4$. The primary distinction between Pathway 1 and Pathway 2 lies in the intermediates formed during the fourth step of the reduction process, CHO^* and COH^*, respectively. The Gibbs free energy change (ΔG) for all reaction steps is less than zero, indicating that each reaction can spontaneously proceed. The rate-determining step (RDS) for Pathway 1 is the formation of $CHOH^*$, with a ΔG of −0.505 eV, while for Pathway 2, it is the formation of COH^*, with a ΔG of −0.123 eV. This suggests that the reduction of CO_2 to CH_4 is more favorable via Pathway 1 through the CHO^* intermediate, due to its lower energy barrier for the RDS. Fig. 12B compares the ΔG during the thermocatalytic reduction of CO_2 using MXene and the ZrOx/MXene composite. The RDS for both MXene and ZrOx/MXene is the step from $CHO^* + H^* \rightarrow CHOH^*$, but the ΔG decreases significantly from 1.834 eV to −0.505 eV upon the introduction of ZrOx. This highlights the catalytic role of Zr^{4+} active sites provided by ZrOx, which substantially lowers the activation energy required for CO_2 reduction, thereby enhancing the efficiency of the CO_2 reduction reaction (CO_2RR).

In summary, DFT calculations indicate that the introduction of Zr-MOF not only provides additional Zr^{4+} catalytic active sites for the thermocatalytic reduction of CO_2, effectively lowering the activation energy of the reaction, but also facilitates the transfer of thermally-generated

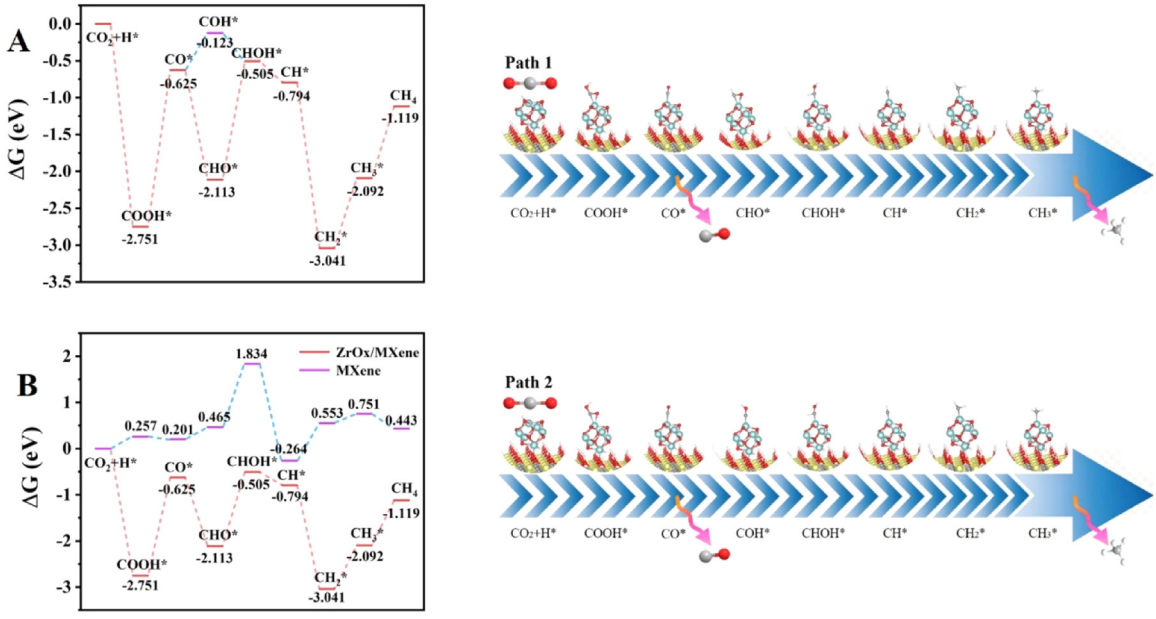

Fig. 12. A. CO_2 reduction reaction pathway; B. Gibbs free energy of CO_2 reduction for MXene and ZrOx/MXene.

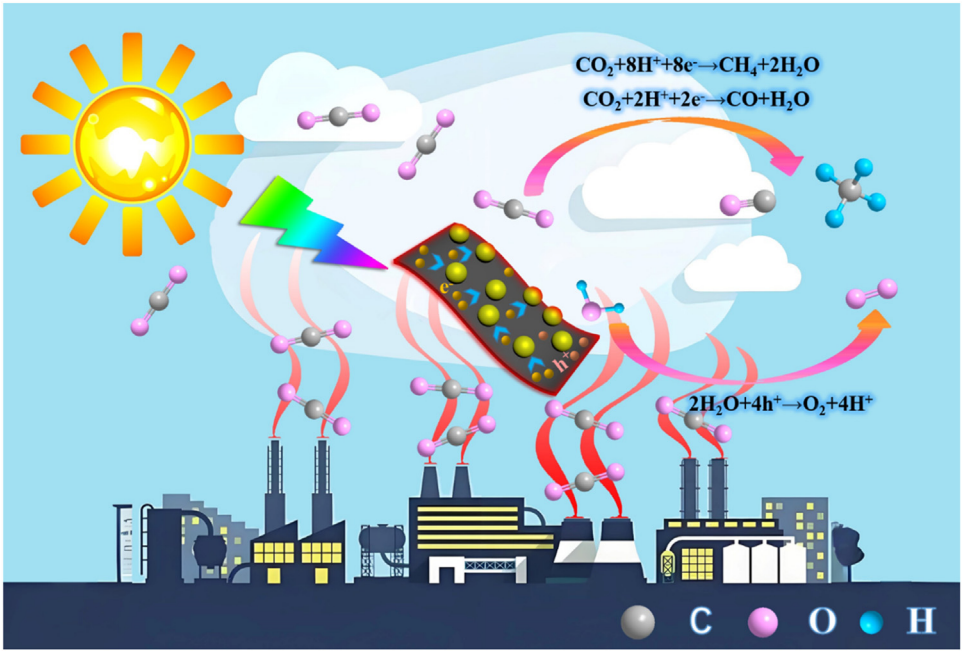

Fig. 13. Mechanism diagram of Zr-MOF/MXene photothermal catalytic reduction of CO_2.

charge carriers, produced by the LSPR effect in MXene, to these Zr^{4+} sites (Fig. 13).

4. Conclusion

In this study, we successfully prepared a composite material with excellent photothermal catalytic performance by combining Zr-MOF (NH_2-UIO-66) with MXene nanosheets through electrostatic self-assembly. This composite material effectively combines the localized surface plasmon resonance (LSPR) effect and high conductivity of MXene with the catalytic active sites of MOF, enabling nearly complete conversion of low-concentration CO_2 in the air and efficient utilization of excess heat from industrial flue gas for high-concentration CO_2 conversion. Further cyclic stability tests also proved that the material has good catalytic stability and can sustainably perform CO_2 reduction reactions. Moreover, the catalytic process, including electron transfer and energy regulation mechanisms, is deeply understood through Density Functional Theory (DFT) calculations, providing a solid theoretical foundation for the high catalytic performance. Based on the above results, the Zr-MOF (NH_2-UIO-66)/MXene composite material not only exhibits significant potential in energy conversion but also underscores its distinct value in carbon cycling and environmental stewardship, thereby advancing the realization of a low-carbon economy. Finally, we are currently designing a novel experimental setup (Figure. S6) for the practical application of CO_2 reduction in atmospheric and industrial flue gas streams, emphasizing the practical relevance and impact of our research.

Declaration of interests

The authors declare that they have no known competing financial interests or personal relationships that could have appeared to influence the work reported in this paper.

CRediT authorship contribution statement

Yang Meng: Writing – original draft, Validation, Methodology, Investigation, Funding acquisition, Formal analysis. **Feng Yue:** Software, Resources, Methodology, Funding acquisition. **Shuo Zhang:** Validation, Resources, Project administration. **Lingji Zhang:** Formal analysis, Data curation. **Cong Li:** Visualization, Software. **Mengke Shi:** Data curation, Conceptualization. **Yongpeng Ma:** Writing – original draft, Project administration, Investigation. **Mario Berrettoni:** Visualization, Supervision, Software. **Xiaojing Zhang:** Writing – review & editing, Writing – original draft, Validation. **Hongzhong Zhang:** Writing – review & editing, Writing – original draft, Visualization, Validation, Supervision.

Data availability

Data available on request from the authors.

Acknowledgements

The authors express their gratitude for the support received from the Henan Collaborative Innovation Center of Environmental Pollution Control.

Supplementary materials

Supplementary material associated with this article can be found, in the online version, at doi:10.1016/j.ccst.2024.100274.

References

Muringa Kandy, M., Rajeev K, A., Sankaralingam, M., 2021. Development of proficient photocatalytic systems for enhanced photocatalytic reduction of carbon dioxide. Sustain. Energy Fuels 5, 12–33. doi:10.1039/d0se01282c.

He, J., Janáky, C., 2020. Recent advances in solar-driven carbon dioxide conversion: expectations versus reality. ACS Energy Lett. 5, 1996–2014. doi:10.1021/acsenergylett.0c00645.

Zhao, S., et al., 2021. Ultrathin NiAl-layered double hydroxides grown on 2D $Ti_3C_2T_x$ MXene to construct core–shell heterostructures for enhanced photocatalytic CO_2 reduction. J. Phys. Chem. C 125, 10207–10218. doi:10.1021/acs.jpcc.1c00017.

Gong, E., et al., 2022. Solar fuels: research and development strategies to accelerate photocatalytic CO_2 conversion into hydrocarbon fuels. Energy Environ. Sci. 15, 880–937. doi:10.1039/d1ee02714j.

Zhai, R., et al., 2023. A review of phosphorus structures as CO_2 reduction photocatalysts. Small 19. doi:10.1002/smll.202207840.

Shang, Z., Feng, X., Chen, G., Qin, R., Han, Y., 2023. Recent advances on single-atom catalysts for photocatalytic CO_2 reduction. Small 19. doi:10.1002/smll.202304975.

Guo, R.t., et al., 2022. Recent advances and perspectives of core-shell nanostructured materials for photocatalytic CO_2 reduction. Small 19. doi:10.1002/smll.202206314.

Dimitriou, I., et al., 2015. Carbon dioxide utilisation for production of transport fuels: process and economic analysis. Energy Environ. Sci. 8, 1775–1789. doi:10.1039/c4ee04117h.

Lim, C.Y.J., Handoko, A.D., Seh, Z.W., 2022. A realistic take on MXenes for electrochemical reduction of carbon dioxide. Diam. Relat. Mater. 130. doi:10.1016/j.diamond.2022.109461.

Jiang, Z., et al., 2020. Filling metal–organic framework mesopores with TiO_2 for CO_2 photoreduction. Nature 586, 549–554. doi:10.1038/s41586-020-2738-2.

Fang, S., et al., 2023. Photocatalytic CO_2 reduction. Nat. Rev. Methods Primers 3. doi:10.1038/s43586-023-00243-w.

Li, X., Yu, J., Jaroniec, M., Chen, X., 2019. Cocatalysts for Selective Photoreduction of CO_2 into Solar Fuels. Chem. Rev. 119, 3962–4179. doi:10.1021/acs.chemrev.8b00400.

Davis, S., Nugegoda, D., Tropp, J., Azoulay, J.D., Delcamp, J.H, 2020. Molecular Au(I) complexes in the photosensitized photocatalytic CO_2 reduction reaction. MRS Commun. 10, 252–258. doi:10.1557/mrc.2020.21.

Liu, X., et al., 2022. Nanoarchitectonics of MXene/semiconductor heterojunctions toward artificial photosynthesis via photocatalytic CO_2 reduction. Coord. Chem. Rev. 459. doi:10.1016/j.ccr.2022.214440.

Rehman, Z.U., et al., 2022. Photocatalytic CO_2 reduction using TiO_2-based photocatalysts and TiO_2 Z-scheme heterojunction composites: a review. Molecules 27. doi:10.3390/molecules27072069.

Wang, J., et al., 2022a. A review on TiO_2−x-based materials for photocatalytic CO_2 reduction. Nanoscale 14, 11512–11528. doi:10.1039/d2nr02527b.

Xiong, Z., et al., 2018. A review on modification of facet-engineered TiO_2 for photocatalytic CO_2 reduction. J. Photochem. Photobiol. C 36, 24–47. doi:10.1016/j.jphotochemrev.2018.07.002.

Qi, F., Pu, Y., Wu, D., Tang, X., Huang, Q., 2023. Recent advances and future perspectives of lead-free halide perovskites for photocatalytic CO_2 reduction. Chem. Rec. 23. doi:10.1002/tcr.202300078.

Chen, X., et al., 2022. Bromo- and iodo-bridged building units in metal-organic frameworks for enhanced carrier transport and CO_2 photoreduction by water vapor. Nat. Commun. 13. doi:10.1038/s41467-022-32367-0.

Wang, Z., et al., 2022b. Selective CO_2 photoreduction to CH_4 via $Pd^{\delta+}$-assisted hydrodeoxygenation over CeO_2 nanosheets. Angew. Chem. Int. Ed. 61. doi:10.1002/anie.202203249.

Chen, W., et al., 2020. Ultrathin Co-Co LDHs nanosheets assembled vertically on MXene: 3D nanoarrays for boosted visible-light-driven CO_2 reduction. Chem. Eng. J. 391. doi:10.1016/j.cej.2019.123519.

Wu, Z., et al., 2021. Niobium and titanium carbides (MXenes) as superior photothermal supports for CO_2 photocatalysis. ACS Nano 15, 5696–5705. doi:10.1021/acsnano.1c00990.

Zhou, H., et al., 2021. Two-dimensional molybdenum carbide 2D-Mo_2C as a superior catalyst for CO_2 hydrogenation. Nat. Commun. 12. doi:10.1038/s41467-021-25784-0.

Crake, A., Christoforidis, K.C., Kafizas, A., Zafeiratos, S., Petit, C., 2017. CO_2 capture and photocatalytic reduction using bifunctional TiO_2/MOF nanocomposites under UV–vis irradiation. Appl. Catal. B 210, 131–140. doi:10.1016/j.apcatb.2017.03.039.

Wang, Z., et al., 2022c. Alkanolamine intercalation assisted liquid phase exfoliation of titanium carbide MXene nanosheets for highly efficient photocatalytic CO_2 reduction. J. Mol. Liq. 367. doi:10.1016/j.molliq.2022.120578.

Han, J., et al., 2022. Bioinspired iron porphyrins with appended poly-pyridine/amine units for boosted electrocatalytic CO_2 reduction reaction. eScience 2, 623–631. doi:10.1016/j.esci.2022.06.003.

Low, J., Zhang, L., Tong, T., Shen, B., Yu, J., 2018. TiO_2/MXene Ti_3C_2 composite with excellent photocatalytic CO_2 reduction activity. J. Catal. 361, 255–266. doi:10.1016/j.jcat.2018.03.009.

Ma, W., et al., 2023. Synergistic interplay of dual-active-sites on metallic Ni-MOFs loaded with Pt for thermal-photocatalytic conversion of atmospheric CO_2 under infrared light irradiation. Angew. Chem. Int. Ed. 62. doi:10.1002/anie.202313784.

Yue, F., et al., 2024. Electro-assisted photocatalytic reduction of CO_2 in ambient air using Ag/TNTAs at the gas-solid interface. Materials Reports: Energy doi:10.1016/j.matre.2024.100269.

Schäppi, R., et al., 2021. Drop-in fuels from sunlight and air. Nature 601, 63–68. doi:10.1038/s41586-021-04174-y.

Zoller, S., et al., 2022. A solar tower fuel plant for the thermochemical production of kerosene from H_2O and CO_2. Joule 6, 1606–1616. doi:10.1016/j.joule.2022.06.012.

Wang, Z., et al., 2021. Generation mechanism and emission reduction measures of CO_x in sintering flue gas. Sintering and Pelletizing doi:10.13403/j.sjqt.2021.01.003.

Wu, T., et al., 2020. Carbon capture technology in cement plant. Cem. Technol. doi:10.19698/j.cnki.1001-6171.20204090.

Yuan, B., et al., 2021. Non-dispersive infrared CO_2 breathing gas sensor based on differential absorption detection technology. Journal of Chongqing University of Posts and Telecommunications (Natural Science Edition) doi:10.3979/j.issn.1673-825X.201903040073.

Liao, J., et al., 2021. Generation and governance way of CO in sintering flue gas: formation mechanism and emission law. Sintering and Pelletizing doi:10.13403/j.sjqt.2021.02.016.

Liu, H., et al., 2024. Research on emission characteristics, testing, and capture technology of CO_2 from industrial flue gas. Power Generation Technol. doi:10.12096/j.2096-4528.pgt.21126.

Gun, J., et al., 2023. Progress in membrane technology for removing carbon dioxide from flue gas. Modern Chemical Industry doi:10.16606/j.cnki.issn0253-4320.2023.S1.017.

Trickett, C.A., et al., 2017. The chemistry of metal–organic frameworks for CO_2 capture, regeneration and conversion. Nat. Rev. Mater. 2. doi:10.1038/natrevmats.2017.45.

Tian, P., et al., 2019. Enhanced charge transfer for efficient photocatalytic H_2 evolution over UiO-66-NH_2 with annealed $Ti_3C_2T_x$ MXenes. Int. J. Hydrogen Energy 44, 788–800. doi:10.1016/j.ijhydene.2018.11.016.

Zhuang, X., et al., 2023. Recent progress of MOF/MXene-based composites: synthesis, functionality and application. Coord. Chem. Rev. 490. doi:10.1016/j.ccr.2023.215208.

Venkateswarlu, S., et al., 2023. Recent progress on MOF/MXene nanoarchitectures: a new era in coordination chemistry for energy storage and conversion. J. Energy Chem. 86, 409–436. doi:10.1016/j.jechem.2023.07.044.

Huang, K., Lv, C., Li, C., Bai, H., Meng, X., 2023. Ti_3C_2 MXene supporting platinum nanoparticles as rapid electrons transfer channel and active sites for boosted photocatalytic water splitting over g-C_3N_4. J. Colloid Interface Sci. 636, 21–32. doi:10.1016/j.jcis.2022.12.169.

Pang, J., et al., 2023. Construction of core–shell MOF@COF hybrids with a Z-scheme heterojunction for efficient visible light photocatalysis. Catal. Sci. Technol. 13, 6198–6210. doi:10.1039/d3cy00869j.

Liu, H., et al., 2021. Boosting the photocatalytic degradation of ethyl acetate by a Z-scheme Au–TiO_2@NH_2-UiO-66 heterojunction with ultrafine Au as an electron mediator. Environ. Sci. Nano 8, 2542–2553. doi:10.1039/d1en00225b.

Xu, D., Li, Z., Li, L., Wang, J., 2020. Insights into the photothermal conversion of 2D MXene nanomaterials: synthesis, mechanism, and applications. Adv. Funct. Mater. 30. doi:10.1002/adfm.202000712.

Ha, M.N., Lu, G., Liu, Z., Wang, L., Zhao, Z., 2016. 3DOM-$LaSrCoFeO_6-\delta$ as a highly active catalyst for the thermal and photothermal reduction of CO_2 with H_2O to CH_4. J. Mater. Chem. A 4, 13155–13165. doi:10.1039/c6ta05402a.

Yang, Z., et al., 2023. The synergy of Ni doping and oxygen vacancies over CeO_2 in visible light-assisted thermal catalytic methanation reaction. Appl. Surf. Sci. 615. doi:10.1016/j.apsusc.2022.156311.

Mon, M., et al., 2018. Synthesis of densely packaged, ultrasmall Pt^02 clusters within a thioether-functionalized MOF: catalytic activity in industrial reactions at low temperature. Angew. Chem. Int. Ed. 57, 6186–6191. doi:10.1002/anie.201801957.

Castells-Gil, J., et al., 2021. Unlocking mixed oxides with unprecedented stoichiometries from heterometallic metal-organic frameworks for the catalytic hydrogenation of CO_2. Chem Catalysis 1, 364–382. doi:10.1016/j.checat.2021.03.010.

Liu, L., et al., 2016. Thermochemical conversion of CO_2 into CH_4 using oxygen deficient $NiFe_2O_4-\delta$ with unique selectivity. RSC Adv. 6, 83814–83819. doi:10.1039/c6ra20473b.

Shen, H., et al., 2022. Identifying the roles of Ce^{3+}−OH and Ce−H in the reverse water-gas shift reaction over highly active Ni-doped CeO_2 catalyst. Nano Res. 15, 5831–5841. doi:10.1007/s12274-022-4207-8.

Stangeland, K., Navarro, H.H., Huynh, H.L., Tucho, W.M., Yu, Z., 2021. Tuning the interfacial sites between copper and metal oxides (Zn, Zr, In) for CO_2 hydrogenation to methanol. Chem. Eng. Sci. 238. doi:10.1016/j.ces.2021.116603.

Kim, A., et al., 2019. Mesoporous TiO_2 support materials for Ru-based CO_2 methanation catalysts. ACS Appl. Nano Mater. 2, 3220–3230. doi:10.1021/acsanm.9b00518.

Bahmanpour, A.M., et al., 2019. Cu–Al spinel as a highly active and stable catalyst for the reverse water gas shift reaction. ACS Catal. 9, 6243–6251. doi:10.1021/acscatal.9b01822.

Zhang, X., et al., 2016. Highly dispersed copper over β-Mo_2C as an efficient and stable catalyst for the reverse water gas shift (RWGS) reaction. ACS Catal. 7, 912–918. doi:10.1021/acscatal.6b02991.

Kattel, S., et al., 2016. CO_2 hydrogenation over oxide-supported PtCo catalysts: the role of the oxide support in determining the product selectivity. Angew. Chem. Int. Ed. 55, 7968–7973. doi:10.1002/anie.201601661.